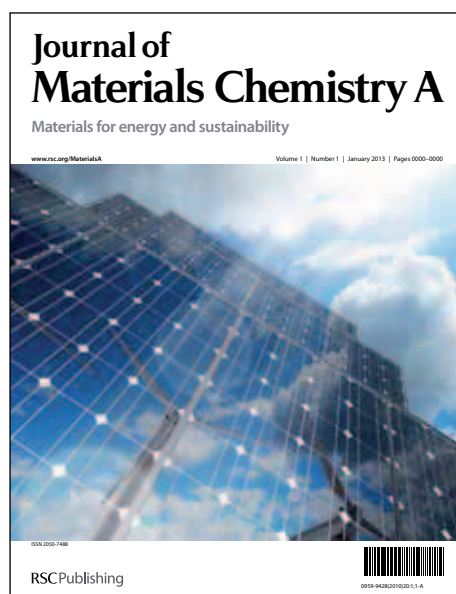


Journal of Materials Chemistry A

Accepted Manuscript



This is an *Accepted Manuscript*, which has been through the RSC Publishing peer review process and has been accepted for publication.

Accepted Manuscripts are published online shortly after acceptance, which is prior to technical editing, formatting and proof reading. This free service from RSC Publishing allows authors to make their results available to the community, in citable form, before publication of the edited article. This *Accepted Manuscript* will be replaced by the edited and formatted *Advance Article* as soon as this is available.

To cite this manuscript please use its permanent Digital Object Identifier (DOI®), which is identical for all formats of publication.

More information about *Accepted Manuscripts* can be found in the [Information for Authors](#).

Please note that technical editing may introduce minor changes to the text and/or graphics contained in the manuscript submitted by the author(s) which may alter content, and that the standard [Terms & Conditions](#) and the [ethical guidelines](#) that apply to the journal are still applicable. In no event shall the RSC be held responsible for any errors or omissions in these *Accepted Manuscript* manuscripts or any consequences arising from the use of any information contained in them.

Cite this: DOI: 10.1039/c0xx00000x

www.rsc.org/xxxxxx

ARTICLE TYPE

Room Temperature Solution Processed Tungsten Carbide as An Efficient Hole Extraction Layer for Organic Photovoltaics

Wei Cui,^{†a} Zhongwei Wu,^{†a} Changhai Liu,^a Mingxing Wu,^b Tingli Ma,^b Suidong Wang,^a Shuit-Tong Lee,^a Baoquan Sun^{*a}

Received (in XXX, XXX) Xth XXXXXXXXX 20XX, Accepted Xth XXXXXXXXX 20XX
DOI: 10.1039/b000000x

We demonstrated tungsten carbide (WC) as an efficient anode buffer layer for the high-performance inverted organic solar cell. The devices based on active layers comprising of either poly(3-hexylthiophene) (P3HT) or poly[[4,8-bis[(2-ethylhexyl)oxy]benzo[1,2-b:4,5-b']dithiophene-2,6-diyl][3-fluoro-2-[(2-ethylhexyl)carbonyl]thieno[3,4-b]thiophenediyl]] (PTB7) mixed with fullerene derivatives had achieved power conversion efficiencies (PCEs) of 3.83% and 8.04%, respectively. The WC layer was deposited onto the active layer from a surfactant-free nanoparticle alcohol solution, because the buffer layer was functionalized well without any requirement for the oxygen-plasma or annealing treatment, which simultaneously allowed optimum photogenerated charge-carrier collection in an inverted structure device. The WC-based device displayed an improved stability performance compared with the MoO₃-based one. The anode buffer layer introduced here was easy to implement and compatible with solution processed organic photovoltaics, and therefore applicable for potential cost-effective manufacturing processes.

I. Introduction

Organic solar cells have achieved rapid progress in the last two decades by optimizing the morphology of active layers, designing novel organic molecules and tailoring device structures¹⁻⁵. Indium tin oxide (ITO) has been discovered as a ubiquitous transparent electrode material for hole extraction in organic solar cells. However, a direct charge extraction into ITO in an organic solar cell is usually inefficient due to energetic mismatch between organic molecular and ITO. Therefore, a buffer layer such as poly(3,4-ethylenedioxythiophene):poly(styrenesulfonate) (PEDOT:PSS) has been introduced onto an ITO surface before the active layer deposition in order to provide a bridge at the interface as well as smoothing the rough ITO film^{6,7}. However, both hygroscopic and acid natures of PEDOT:PSS can result in the degradation of device performances^{8,9}. In addition, PEDOT:PSS displays a work function of ~5.1 eV, which is not deep enough to offer a large internal electric field⁶. One approach by fabricating an inverted device structure has been developed to circumvent these problems¹⁰. The transition metal oxides such as molybdenum oxide (MoO₃)^{11,12}, silver oxide (Ag_xO)¹³, chromium oxide (Cr₂O₃)¹⁴, vanadium oxide (V₂O₅)¹⁵, nickel oxide (NiO_x)^{16,17}, tungsten oxide (WO₃)¹⁸⁻²⁰, and rhenium oxide (ReO₃)²¹ exhibit large work functions because of their natures of strongly p-doped by oxygen vacancy, which are commonly applied as anode buffer layers for high efficient collection of photogenerated charge carriers in inverted organic solar cells. Furthermore, relatively stable metal oxide-based devices have been demonstrated.

To the best of our knowledge, the metal oxides discussed above have so far been generally fabricated by vacuum thermal deposition, which may be a drawback for future large-scale all-solution manufacturing processing. Alternatively, various solution-based methods have been investigated to fabricate the metal oxide films^{12,15,17,22-24}. The sol-gel technique has been extensively employed for transition metal oxide films^{4,17,25-27}. However, most of the methods require post annealing processes to allow the precursors to thermally decompose into metal oxide which may be incompatible to inverted organic solar cells. Many organic molecules cannot tolerate the high temperature annealing process. Alternatively, solutions comprising of metal oxide nanoparticles have been employed before depositing anode films onto active layer films, however, post-annealing is still required to fabricate hole collection layers²²⁻²⁴.

Tungsten carbide (WC) is a kind of material with specific properties such as high corrosion resistance, electrical conductivity and excellent catalytic activity²⁸. The extraordinary electronic properties of WC are gained from its ionic contribution characterized by the charge transfer from metal atoms to non-metal ones²⁹. Those electronic properties lead to the initial state effects including change of the coordination of the substrate atoms, which usually lower the surface potential³⁰. As a chemical reaction catalyst, it is a potential substitute of expensive noble metals because of its low cost and high catalytic selectivity. The high catalytic activity of WC is ascribed to its positively charged transition metal in the carbide. The direction of charge transfer is

from metal to carbon. Recently, WC has been applied as the counter electrode for dye sensitized solar cells, and a comparable performance has been achieved in comparison with widely-used platinum^{31, 32}.

Here, we demonstrated the WC layers, fabricated from an alcohol WC nanoparticle suspension, could undertake the role as an efficient anode buffer layer. The devices based on WC layers display superior performance compared to those based on thermally evaporated molybdenum oxide (e-MoO₃). The WC film could be readily formed onto the film comprising of either poly(3-hexylthiophene) (P3HT) or poly[[4,8-bis[(2-ethylhexyl)oxy]benzo[1,2-b:4,5-b']dithiophene-2,6-diyl][3-fluoro-2-[(2-ethylhexyl)carbonyl]thieno[3,4-b]thiophenediyl]] (PTB7) mixed with fullerene derivatives by spin-coating. The prepared anode buffer layer did not require any additional thermal treatment for functional hole extraction in the inverted organic solar cell.

II. Experimental

A. Preparation of WC solution

Crystalline WC powder was purchased from CW-Nano Company (Shanghai, China). WC powder could be dispersed in isopropanol (IPA) with a concentration of 5 mg/mL by an ultrasonic cell crusher (BILON 92-IID). After high energy processing, the WC suspensions were diluted by IPA for device fabrication.

B. Fabrication and characterization of OPVs

The glass substrate coated with patterned ITO was cleaned thoroughly and then exposed under UV-ozone for 15 min. The sol-gel zinc oxide (ZnO) precursor was deposited onto the ITO substrate and then annealed at 150 °C for 90 min in air. Next, an active layer of P3HT: [6,6]-phenyl-C61-butyric acid methyl ester (PC₆₁BM) or PTB7: [6,6]-phenyl-C71-butyric acid methyl ester (PC₇₁BM) was cast upon the ZnO buffer layer, respectively. The weight ratios of P3HT:PC₆₁BM (in dichlorobenzene) and PTB7:PC₇₁BM (in chlorobenzene with 3% 1,8-diiodooctane) were 1:0.8 and 1:1.5, respectively. Subsequently, WC suspensions were deposited onto the active layer by repeated spin-coating for multiple times from one to three. Finally, the patterned silver electrode was deposited by thermal evaporation using Mini-Spectros high vacuum system (Kurt J. Lesker). The device area was 8.25 mm² restricted by shadow mask.

C. Characterization of WC solution and films

The UV-vis absorbance and transmittances were recorded on analytik jena SPECORD S600. Zeta potentials were acquired using a particle size analyser (Malvern Nano-ZS90). X-ray diffraction (XRD) measurements were carried out using an X-ray powder diffractometer (PANalytical Empyrean). The topography and the surface potentials were performed by atomic force microscopy (AFM) (Veeco, Multimode V). The film thicknesses were acquired with Alpha SE spectroscopic ellipsometer (J.A. Woollam). The work function of WC was obtained by pressing WC powder on an indium substrate and measuring by X-ray photoelectron spectrometer (KRATOS Analytical). The particle sizes were characterized by a FEI Tecnai G2 F20

transmission electron microscope (TEM). The photoluminescence (PL) lifetime was measured by time-correlated single-photon counting (TCSPC) in air by HORIBA-fm-2015 for P3HT both with and without WC or e-MoO₃. The cross-section HRSEM image was measured by Zeiss Supra 55. The device performances were characterized under simulated air mass (AM) 1.5 G irradiation at 100 mW/cm² using a Xe lamp-based solar simulator (Newport 91160). The light intensity was calibrated using a Newport standard silicon solar cell 91150.

III. Results and discussion

A high-intensity ultrasonication method was used to shred WC bulks into nanoparticles. WC particles displayed a size distribution ranging from 20 nm to 200 nm after high-intensity ultrasonication treatment, as shown in **Figure 1** (a) (b) and **Figure S1** (a), while the WC bulk before treatment was several microns, as shown in **Figure S1** (b). AFM images were measured to characterize the surface of the nanoparticles. The samples were prepared by spin-coating the WC nanoparticles on a polished silicon substrate. As shown in **Figure 2** (b) and (c), the AFM cross-sectional line profiles displayed heights of a few nm and widths of 40-150 nm, implying that the WC nanoparticles exhibited smooth surface, which might possess the ability to form uniform films. The corresponding three-dimensional AFM image was shown in **Figure S2**. This material was preferred to attach to the substrate smoothly. The preferred orientation resulted from the capillary effect in the spin-coating process³³. The smooth surface were also explained by the different contrast existed in the TEM image of **Figure 1** (a) and **Figure S1** (c). The insert image in **Figure 1** (a) showed the labelled lattice direction corresponding to the (001) planes of WC, which was confirmed by the selected area electron diffraction (SAED) image inserted in **Figure 1** (b).

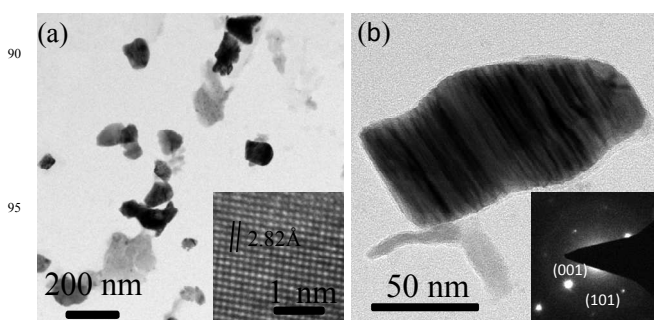


Figure 1 (a, b) TEM images of commercial bulk WC after high-intensity ultrasonication process. (Inserts) High-resolution TEM image and selected area electron diffraction (SAED) image of (b). The labelled distance of 2.82 Å corresponds to the (001) lattice spacing, which was confirmed in SAED image.

Notably, after ultrasonication, the WC particles in isopropanol could be well dispersed, forming a stable suspension. **Figure 2** (d) revealed the UV-vis absorption spectra of WC in isopropanol solvent and the inset photograph was the WC solution after ultrasonication with a concentration of ~0.5 mg/mL. It was clearly indicated that the suspension displayed good stability. The small nanoparticles in isopropanol did not show any obvious

precipitation in two weeks. To investigate dispensability of the WC suspensions, the Zeta potentials were measured before and after ultrasonication. As shown in **Figure S3**, the surface potential values of WC nanoparticles changed from initial -18.3 mV to final -41.0 mV. The Zeta potential values had grown one times after post-treatment, approximately. The results indicated that the nanoparticles were highly charged, thereby improving the dispensability in IPA.

X-ray diffraction (XRD) was introduced to analyse the crystalline structure of WC. As shown in **Figure S4**, the diffraction peaks in 31.05, 35.22, 47.88, 63.64, 65.33, 72.71, 75.14, 76.70 and 83.68 degree could be assigned to the (001), (100), (101), (110), (002), (111), (200), (102) and (201) crystal planes, respectively, according to the standard diffraction pattern of bulk WC (no. 89-2727, PDF-2 Database). And no crystal transformation was observed after ultrasonication process in the hexagonal crystals. The full width at half maximum slightly increased after ultrasonication, which indicated that the sizes of the WC nanoparticles decreased, as shown in **Figure S4**. The transmittance spectra of WC and MoO₃ films were plotted in **Figure S5**, in which the WC films exhibited weaker absorption than that of the MoO₃ film especially below 400 nm.

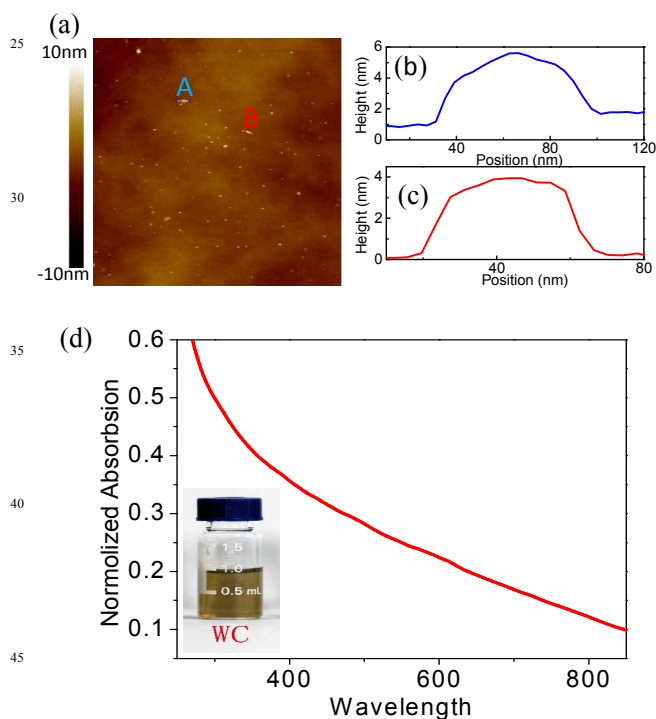


Figure 2 (a) AFM image of the WC nanoparticles on polished silicon substrate. The image size was 2 μm x 2 μm . (b) and (c) AFM cross-sectional line profiles of spot A and B in Figure 1 (a), respectively. (d) The UV-vis absorption spectra of WC suspension after ultrasonication. (Inset) Photograph of the WC solution after ultrasonication with a concentration of ~ 0.5 mg/mL.

Energy matching of the frontier orbital energies of the photo-active layer to the inter-layer is essential in order to establish electronic equilibrium and minimize charge extraction barrier. The difference of surface potential between the active layer and

the film fabricated by the WC nanoparticles was evaluated using scanning Kelvin probe microscopy (SKPM) in ambient atmosphere. The experimental setup was according to the previous report³⁴, in which the surface potentials of P3HT:PC₆₁BM films with and without the WC nanoparticles were measured respectively. **Figure 3** (a) and (b) were the topographic images of P3HT:PC₆₁BM and P3HT:PC₆₁BM/WC, while **Figure 3** (c) and (d) were the corresponding surface potential images. The SKPM measurement of the surfaces exhibited 122 ± 37 eV more negative in average surface potential occurring after spin-coating the WC nanoparticles. The results indicated an electric dipole moment with the negative charge ended pointing toward P3HT:PC₆₁BM and the positive charge ended pointing toward the silver electrode, as shown in **Figure S6**. The microscopic electrical field between the P3HT:PC₆₁BM layer and the anode was energetically favourable for the charge extraction. However, WC displayed a work function of 4.7 eV measured by UPS, as shown in **Figure S7**, which is lower than that of MoO₃.

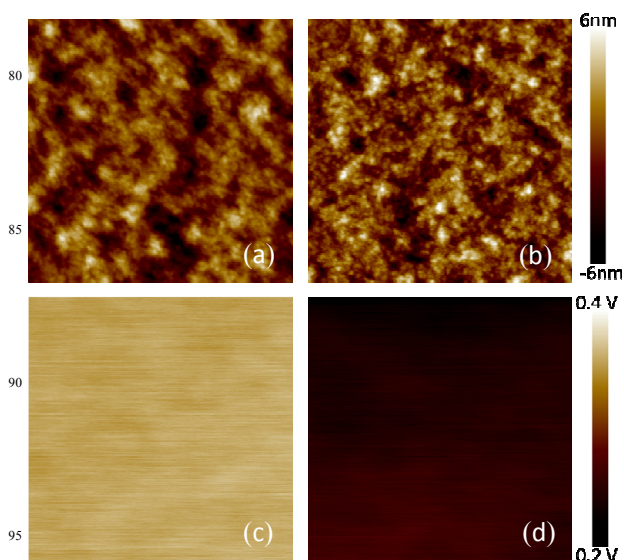


Figure 3 Scanning Kelvin probe microscope to probe the electric dipole moment of WC interlayer on P3HT:PC₆₁BM. Topographic image of (a) P3HT:PCBM and (b) P3HT:PCBM/WC. The surface potential image of (c) P3HT:PCBM and (d) P3HT:PCBM/WC. The size of all the images was 2 μm x 2 μm .

The film quality of buffer layers played an important role on the device performance. A thin and compacted film was necessary to allow WC to fully functionalize as an efficient hole extraction layer. The film quality was determined by AFM images, as shown in **Figure 4**. The P3HT:PC₆₁BM film with and without WC displayed dramatically different topographic images. Without WC, there were obvious interpenetrating networks in the P3HT:PC₆₁BM film, as shown in **Figure 4** (a) and (c). While with WC, the feature became vague since P3HT:PC₆₁BM was partially covered by the WC nanoparticles (**Figure S8** (c) and (d)). When the WC film was fabricated by spin-coating for three times, the feature disappeared, implying that a uniform and smooth WC film was formed, as shown in **Figure 4** (b) and (d). If the WC was only deposited by solution spin-coating once or twice, there would be pinhole regions where silver could directly contact with

P3HT:PC₆₁BM. Here, the multiple spin-coating process was utilized to obtain a continuous WC film. The film thickness was ~5-15 nm determined by ellipsometer. In addition, pristine isopropanol was spin-coated on the active layers in order to exclude the solvent effect on the film quality of the P3HT:PCBM films, and the AFM images (Figure S9) indicated that isopropanol had little influence on the surface morphology. In addition, the SEM image in Figure S10 (a) exhibited a uniform WC film deposited on P3HT:PCBM by spin-coating for 3 times. The carbon signal resulted from P3HT, PCBM and the WC nanoparticles, while the tungsten signal was mere from WC. Figure S10 (c) suggested the WC film was uniform and continuous, since if the nanoparticles were partially covered the active layer, a randomly distributed spots for tungsten element signal were expected instead of uniform and continuous ones.

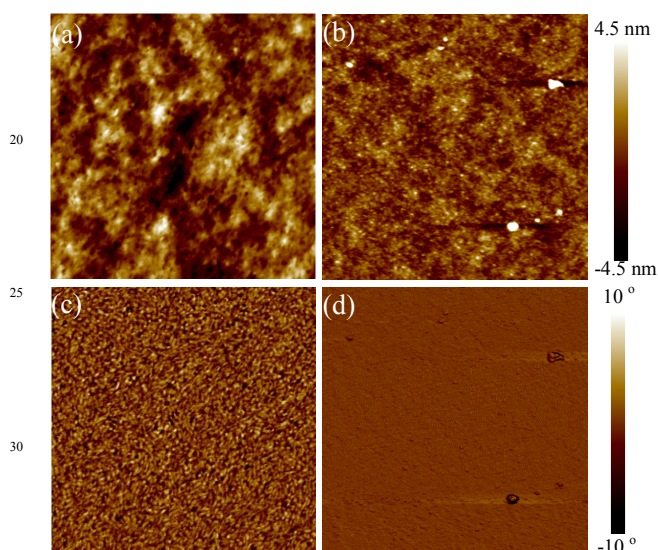


Figure 4 AFM images of P3HT:PC₆₁BM films without (a) Height, (c) Phase and with WC film (b) Height, (d) Phase. The spin-coating WC steps were repeated three times.

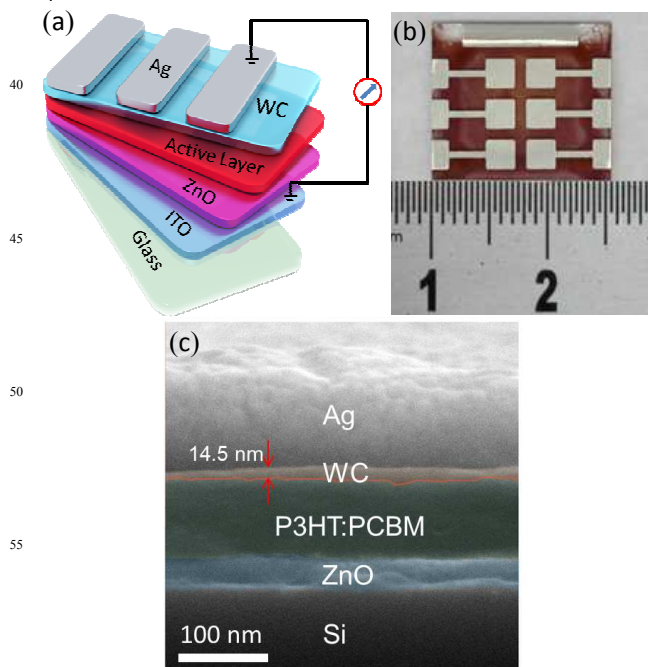


Figure 5 (a) The Architecture of the inverted organic solar cell. ZnO acted as the cathode buffer layer. The anode buffer layer can be traditional e-MoO₃ or new-developed solution processed WC nanoparticles film. The active layer was blend of either P3HT:PC₆₁BM or PTB7:PC₇₁BM. (b) The photograph of the device based on ITO/ZnO/P3HT:PC₆₁BM/WC/Ag structure. (c) HR-SEM cross-sectional image of the optimized device configuration. The different layer were tinted with colour guideline.

To assess the WC nanoparticles as a hole transporting layer, P3HT:PC₆₁BM and PTB7:PC₇₁BM were utilized as photo-active layers, since both of them were well characterized systems. The structure of the inverted bulk heterojunction devices was illustrated in Figure 5 (a), while the photograph of the real made-up device was shown in Figure 5 (b). The energy band structures of the devices were illustrated in Figure S11. The high work function metal oxides, which acted as anode buffer layers, were replaced with WC. This inter-layer was deposited by solution spin-coating process at room temperature. An extra-annealing process was unnecessary before an anode electrode deposition, enabling easy processibility over large area by roll to roll processing. To be able to characterize the each layer thickness of the device, high resolution scanning electron microscope (HR-SEM) was introduced. Figure 5 (c) showed the HRSEM cross-section image of the device, in which the thickness of WC layer was ~14.5 nm, which was consistent with the one of 5-15 nm measured with ellipsometer. The images inserted in Figure 6 (a) and (b) displayed the chemical structures of P3HT and PTB7. The WC films worked as the anode buffer layer for hole transporting. For the devices based on various active layers, the electrons and holes moving directions were the same.

Figure 6 (a) exhibited the current density-voltage (J-V) electric output characteristics of the representative devices based on P3HT:PC₆₁BM with different anode buffer layers between spin-coated WC and e-MoO₃. The short-circuit current density (J_{sc}), the open-circuit voltage (V_{oc}), the fill factor (FF) and the power conversion efficiency (PCE) of all the devices were summarized in Table 1, and were recorded on 20 separate specimens for each type of cells. The reference device with e-MoO₃ exhibited a PCE of 3.73% ($V_{oc} = 0.61$ V, $J_{sc} = 9.08$ mA/cm², FF = 0.67), which was comparable with those reported performances^{12, 13}. The device based on the WC anode buffer layer displayed a PCE 3.83%, with a V_{oc} of 0.61 V, a J_{sc} of 9.52 mA/cm², and a FF of 0.66, exhibiting a slight enhancement in PCE over the reference. Figure 6 (c) showed typical external quantum efficiency (EQE) data for devices based on WC and e-MoO₃, which noted that the EQE response of the WC-based device was slightly enhanced than that of the reference. The stability data of device performances were also plotted in Figure S12, in which the WC-based device reserved ~90% of initial PCE, while MoO₃-based device only exhibited ~82% of initial one after 650 hours air exposure. The WC-based device demonstrated an improved stability, which might be ascribed to the inert and stable chemical properties of WC. The results implied that WC could functionalize better than the reference of e-MoO₃ as anode buffer

layers in P3HT:PC₆₁BM devices.

PTB7:PC₇₁BM was used to act as an active layer to evaluate WC being a general buffer layer for the inverted organic solar cells as well, as shown in **Figure 6** (b). All the electrical output characteristics based on PTB7:PC₇₁BM were summarized in **Table 1**. The WC-based device demonstrated a PCE of 8.04% ($V_{oc} = 0.72$ V, $J_{sc} = 15.98$ mA/cm², FF = 0.70), which displayed superior performance to the device with e-MoO₃ as a hole transporting layer ($V_{oc} = 0.73$ V, $J_{sc} = 15.24$ mA/cm², FF = 0.70, PCE = 7.82%). The J_{sc} improvement of the WC-based device was supported by the EQE data illustrated in **Figure 6** (d), in which the highest measured EQE of this device was 76% at 660 nm.

This result further confirmed that solution-processed WC could be an efficient anode buffer layer to replace thermal evaporated high work function metal oxides. In both **Figure 6** (c) and (d), the EQE values were slightly improved, especially in the range of 350–400 nm, which resulted from the different transmittances between MoO₃ and WC films. The incident light partially passed through the active layer as well as the hole extraction layer, then was reflected by silver electrode into the active layer to generate the charges. And the absorbed light in MoO₃ and WC did not contribute any photocurrent. The WC film displayed weaker absorption below 400 nm as shown in **Figure S6**, and more light was harvested by the active layer, which led to an enhanced EQE. However, the improved EQE at 500 nm was still unclear yet.

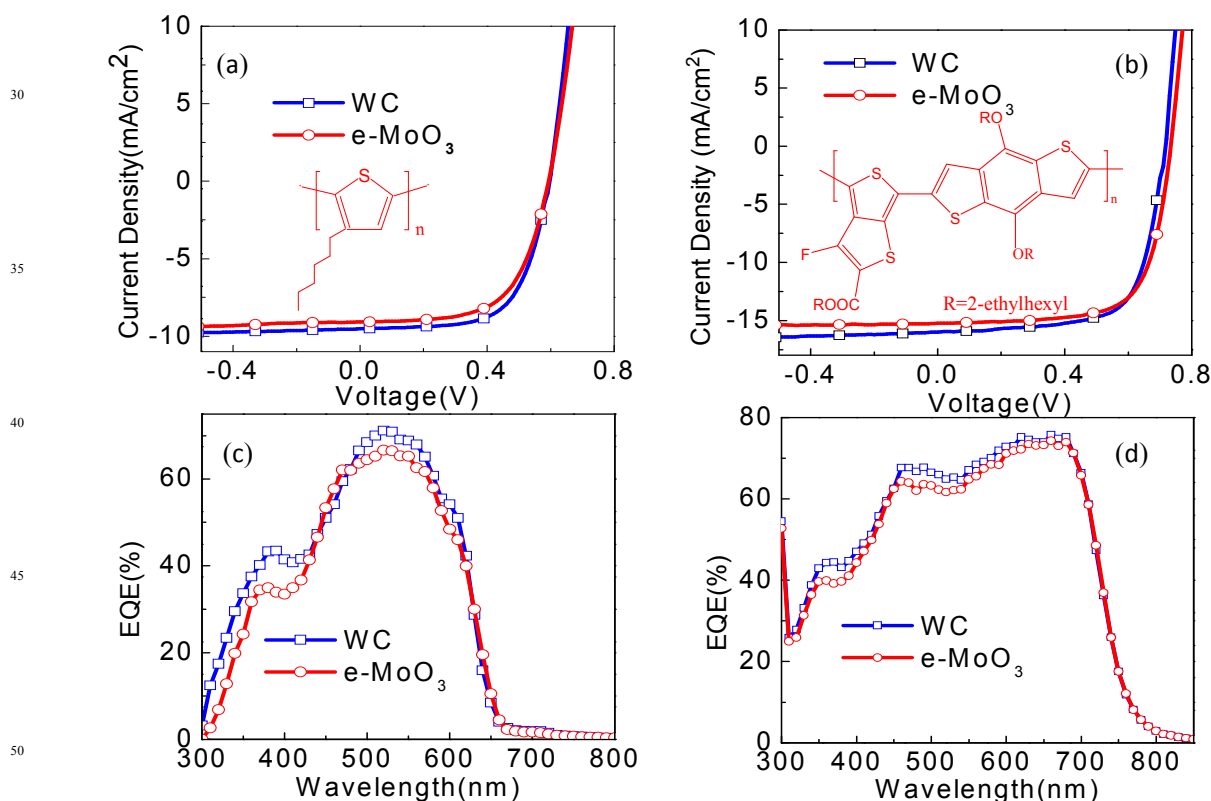


Figure 6 J-V data for inverted solar cells based on (a) P3HT:PC₆₁BM and (b) PTB7:PC₇₁BM under solar simulated A.M. 1.5 light illumination with at 100 mW/cm². The chemical structures of poly(3-hexylthiophene) (P3HT) and poly[[4,8-bis[[2-ethylhexyl]oxy]benzo[1,2-b:4,5-b']dithiophene-2,6-diyl][3-fluoro-2-[(2-ethylhexyl)carbonyl]thieno[3,4-b]thiophenediyl]] (PTB7) were inset in (a) and (b), respectively. The spin-coating WC steps were repeated for three times. MoO₃ was fabricated by vacuum thermal evaporation (e-MoO₃).

	V_{oc} (V)	J_{sc} (mA cm ⁻²)	FF	PCE (%)
P3HT:PC ₆₁ BM/WC	0.61 0.60 (±0.01)	9.52 9.23 (±0.38)	0.66 0.65 (±0.012)	3.83 3.72 (±0.11)
P3HT:PC ₆₁ BM/e-MoO ₃	0.61 0.61 (±0.01)	9.08 8.95 (±0.25)	0.67 0.66 (±0.018)	3.73 3.69 (±0.07)
PTB7:PC ₇₁ BM/WC	0.72 0.72 (±0.01)	15.98 16.06 (±0.43)	0.70 0.70 (±0.008)	8.04 7.96 (±0.21)
PTB7:PC ₇₁ BM/e-MoO ₃	0.73 0.73 (±0.01)	15.24 15.06 (±0.17)	0.70 0.69 (±0.018)	7.82 7.63 (±0.33)

^aData and statistics based on 20 cells of each type. ^bNumbers in bold are the maximum recorded values.

Table 1 Summary of electric output characteristics of the inverted solar cells based on P3HT:PC₆₁BM and PTB7:PC₇₁BM.

As discussed previously, the compacted WC film was dispensable to achieve high device performance. The electrical output characteristics of the devices based on the WC films fabricated by multiple spin-coating times were plotted in **Figure S13** and summarized in **Table S1**. The devices based on the WC films fabricated by deposition for three times exhibited the best PCEs both in P3HT:PC₆₁BM and PTB7:PC₇₁BM devices, which was consistent with our previous observation in which a dense and compacted WC layer was formed by repeated deposition for three times. In addition, it has been very recently reported that the solvent treatment (methanol) on organic materials could enhance the charge extraction³⁴. Pristine isopropanol was also deposited on the active layers to exclude its effect on the device performances. As shown in **Figure S14** and **Table S2**, the devices based on isopropanol treated (without MoO₃) displayed very poor performances, implying that isopropanol had very little effect on the device performance.

Both devices displayed similar V_{oc} regardless of WC or e-MoO₃ as anode buffer layers. A generally accepted estimate for the V_{oc} of a polymer solar cell was given by the offset between the highest occupied molecular orbital (HOMO) level of donor and the lowest unoccupied molecular orbital (LUMO) level of acceptor minus 0.3 V, which was ascribed to the polaron pair binding energy^{35, 36}. The observation of similar V_{oc} of the devices indicated that different anode buffer layers had no influence on HOMO level of P3HT and LUMO level of PC₆₁BM. In addition, WC acted as a similar function of e-MoO₃ as the hole extraction layer as well as doping effect, such as graphene oxide³⁷.

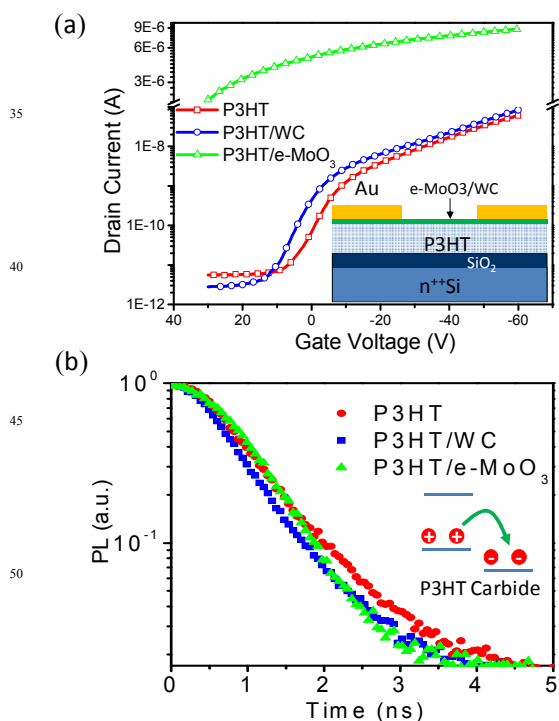


Figure 7 (a) Transfer characteristics of thin-film transistors based on P3HT as active layers with and without WC or e-MoO₃ layers, respectively. The device structure was inset. (b) The photoluminescence lifetime spectra for P3HT films with and without WC or e-MoO₃ layers above, respectively. The charge transfer process model was inset.

In order to investigate WC doping effecting on P3HT mobility, thin-film field effect transistors were fabricated based on P3HT as active layers with and without WC or e-MoO₃ layers. As the transfer characteristics curves shown in **Figure 7** (a), the field effect mobilities was slightly enhanced from $2.9 \times 10^{-4} \text{ cm}^2 \text{V}^{-1} \text{s}^{-1}$ to $5.6 \times 10^{-4} \text{ cm}^2 \text{V}^{-1} \text{s}^{-1}$ after WC deposited on P3HT film. As for e-MoO₃, a mobility of $9.6 \times 10^{-4} \text{ cm}^2 \text{V}^{-1} \text{s}^{-1}$ was obtained. It was implied that there was some doping effect in both WC and MoO₃ cases. In addition, the turn-on voltage shifted more positive direction, indicating there were more extra free holes at zero bias requiring completely depleting. The results can be interpreted by the charge transfer between WC/e-MoO₃ and P3HT. The Fermi level of WC should locate below the ionization potential of P3HT. If a substrate Fermi level falls below an ionization energy of molecules, the number of ionized molecular will increase dramatically.³⁸ The amount of ionized P3HT increased, generating a positive electric layer in the organic layer, which led to a negative shift of the turn-on voltage. To further confirm the charge transfer from the WC buffer layer to the polymer film, we utilized TCSPC to analyse the photoluminescence (PL) lifetime of both pristine P3HT films and P3HT ones with the WC nanoparticles or e-MoO₃ above. The PL lifetime spectra shown in **Figure 7** (b) revealed that a slight decrease in PL lifetime was observed after WC (e-MoO₃) deposition. The results indicated that there was charge transfer taken place at the interface in both WC and MoO₃, which was consistent with the turn-on voltage shifting in TFT device.

IV. Conclusions

In conclusion, the solution-processed WC nanoparticles, which can be dispersed in alcohol solvent easily to form stable suspensions, as a candidate to form an efficient anode buffer layer had been demonstrated for the inverted organic solar cell. The WC film could functionalize well as an anode buffer layer without further post-treatment, which displayed superior device performance regarding to the active layer of P3HT:PC₆₁BM and PTB7:PC₇₁BM. It was indicated that WC could act as a general efficient buffer layer material for the inverted organic solar cells. The anode layer introduced here is easy to implement and compatible with a solution processed organic solar cell, and therefore applicable for potential cost-effective manufacturing processes. This discovery of an efficient anode buffer layer could find use in fully exploiting the potential of various organic electronic device systems.

Notes and references

[*] Author information: bqsun@suda.edu.cn;

[†] Both authors contributed equally to this work.

^a Jiangsu Key Laboratory for Carbon-Based Functional Materials & Devices, Institute of Functional Nano & Soft Materials (FUNSOM) & Collaborative Innovation Center of Suzhou Nano Science and Technology, Soochow University, Suzhou 215123, P. R. China

^b State Key Laboratory of Fine Chemicals, Dalian University of Technology, No. 2 Linggong Road, Ganjingzi District, Dalian City, Liaoning Province, P. R. China 116024

† Electronic Supplementary Information (ESI) available: low resolution TEM image of the WC nanoparticles; AFM topographic 3-dimension

- image; the Zeta potentials of the WC solutions; XRD patterns of WC; the cartoon model of charge transfer at the interface; transmittance spectra of e-MoO₃ and WC films; UPS spectrum of WC film; AFM images and J-V curves of P3HT:PC₆₁BM films with different post-treatment; SEM image of the WC film and the corresponding EDX mapping images; the stability data of the devices base on WC and e-MoO₃ the band structure of devices and the device stability test. See DOI: 10.1039/b000000x/
1. R. Lecover, N. Williams, N. Markovic, D. H. Reich, D. Q. Naiman and H. E. Katz, *ACS Nano*, 2012, **6**, 2865.
 2. W. Ma, C. Yang, X. Gong, K. Lee and A. J. Heeger, *Adv. Funct. Mater.*, 2005, **15**, 1617.
 3. D. Chen, A. Nakahara, D. Wei, D. Nordlund and T. P. Russell, *Nano Lett.*, 2011, **11**, 561.
 4. J. J. Jasieniak, J. Seifert, J. Jo, T. Mates and A. J. Heeger, *Adv. Funct. Mater.*, 2012, **22**, 2594.
 5. A. A. Guilbert, L. X. Reynolds, A. Bruno, A. MacLachlan, S. P. King, M. A. Faist, E. Pires, J. E. Macdonald, N. Stingelin, S. A. Haque and J. Nelson, *ACS Nano*, 2012, **6**, 3868.
 6. H. Frohne, S. E. Shaheen, C. J. Brabec, D. C. Muller, N. S. Sariciftci and K. Meerholz, *Chemphyschem*, 2002, **3**, 795.
 7. H. Park, R. M. Howden, M. C. Barr, V. Bulovic, K. Gleason and J. Kong, *ACS Nano*, 2012, **6**, 6370.
 8. F. So and D. Kondakov, *Adv. Mater.*, 2010, **22**, 3762.
 9. M. P. de Jong, L. J. van Ijzendoorn and M. J. A. de Voigt, *Appl. Phys. Lett.*, 2000, **77**, 2255.
 10. G. Li, C. W. Chu, V. Shrotriya, J. Huang and Y. Yang, *Appl. Phys. Lett.*, 2006, **88**, 253503.
 11. H. Schmidt, H. Flugge, T. Winkler, T. Bulow, T. Riedl and W. Kowalsky, *Appl. Phys. Lett.*, 2009, **94**, 243302.
 12. K. Zilberberg, H. Gharbi, A. Behrendt, S. Trost and T. Riedl, *ACS Appl. Mater. Interfaces*, 2012, **4**, 1164.
 13. W.-J. Yoon and P. R. Berger, *Appl. Phys. Lett.*, 2008, **92**, 013306.
 14. P. Qin, G. Fang, Q. He, N. Sun, X. Fan, Q. Zheng, F. Chen, J. Wan and X. Zhao, *Sol. Energ. Mat. Sol. C.*, 2011, **95**, 1005.
 15. C.-P. Chen, Y.-D. Chen and S.-C. Chuang, *Adv. Mater.*, 2011, **23**, 3859.
 16. M. D. Irwin, D. B. Buchholz, A. W. Hains, R. P. H. Chang and T. J. Marks, *PNAS*, 2008, **105**, 2783.
 17. K. X. Steirer, P. F. Ndione, N. E. Widjonarko, M. T. Lloyd, J. Meyer, E. L. Ratcliff, A. Kahn, N. R. Armstrong, C. J. Curtis, D. S. Ginley, J. J. Berry and D. C. Olson, *Adv. Eng. Mater.*, 2011, **1**, 813.
 18. C. Tao, S. Ruan, G. Xie, X. Kong, L. Shen, F. Meng, C. Liu, X. Zhang, W. Dong and W. Chen, *Appl. Phys. Lett.*, 2009, **94**, 043311.
 19. Z. A. Tan, L. Li, C. Cui, Y. Ding, Q. Xu, S. Li, D. Qian and Y. Li, *J. Phys. Chem. C*, 2012, **116**, 18626.
 20. T. Stubhan, N. Li, N. A. Luechinger, S. C. Halim, G. J. Matt and C. J. Brabec, *Adv. Eng. Mater.*, 2012, **2**, 1433.
 21. D.-H. Kim, T.-M. Kim, W.-I. Jeong and J.-J. Kim, *Appl. Phys. Lett.*, 2012, **101**, 153303.
 22. J. You, C.-C. Chen, L. Dou, S. Murase, H.-S. Duan, S. A. Hawks, T. Xu, H. J. Son, L. Yu, G. Li and Y. Yang, *Adv. Mater.*, 2012, **24**, 5267.
 23. T. Stubhan, T. Ameri, M. Salinas, J. Krantz, F. Machui, M. Halik and C. J. Brabec, *Appl. Phys. Lett.*, 2011, **98**, 253308.
 24. J. Meyer, R. Khalandovsky, P. Görrn and A. Kahn, *Adv. Mater.*, 2011, **23**, 70.
 25. C. Girotto, E. Voroshazi, D. Cheyns, P. Heremans and B. P. Rand, *ACS Appl. Mater. Interfaces*, 2011, **3**, 3244.
 26. T. Yang, M. Wang, Y. Cao, F. Huang, L. Huang, J. Peng, X. Gong, S. Z. D. Cheng and Y. Cao, *Adv. Eng. Mater.*, 2012, **2**, 523.
 27. S. Murase and Y. Yang, *Adv. Mater.*, 2012, **24**, 2459.
 28. S. T. Oyama, ed., *The Chemistry of Transition Metal Carbide and Nitride*, Blackie Academic & Professional, London, 1996.
 29. J. G. Chen, *Chem. Rev.*, 1996, **96**, 1477.
 30. G. A. Benesh and D. A. King, *Chem. Phys. Lett.*, 1992, **191**, 315.
 31. M. Wu, X. Lin, A. Hagfeldt and T. Ma, *Angew. Chem. Int. Ed.*, 2011, **50**, 3520.
 32. M. Wu, X. Lin, Y. Wang, L. Wang, W. Guo, D. Qi, X. Peng, A. Hagfeldt, M. Grätzel and T. Ma, *J. Am. Chem. Soc.*, 2012, **134**, 3419.
 33. M. Xu, T. Liang, M. Shi and H. Chen, *Chem. Rev.*, 2013, **113**, 3766.
 34. H. Zhou, Y. Zhang, J. Seifert, S. D. Collins, C. Luo, G. C. Bazan, T.-Q. Nguyen and A. J. Heeger, *Adv. Mater.*, 2013, **25**, 1646.
 35. C. J. Brabec, A. Cravino, D. Meissner, N. S. Sariciftci, T. Fromherz, M. T. Rispens, L. Sanchez and J. C. Hummelen, *Adv. Funct. Mater.*, 2001, **11**, 374.
 36. K. Vandewal, K. Tvingstedt, A. Gadisa, O. Inganas and J. V. Manca, *Nat. Mater.*, 2009, **8**, 904.
 37. Y. Gao, H.-L. Yip, K.-S. Chen, K. M. O'Malley, O. Acton, Y. Sun, G. Ting, H. Chen and A. K. Y. Jen, *Adv. Mater.*, 2011, **23**, 1903.
 38. M. T. Greiner, M. G. Helander, W.-M. Tang, Z.-B. Wang, J. Qiu and Z.-H. Lu, *Nat. Mater.*, 2012, **11**, 76.

Table of Contents:

